

# EXPERIMENTAL VALIDATION OF A FLUIDIC PITCH LINK MODEL

Shawn M. Treacy  
PhD Candidate

Christopher D. Rahn  
Professor

Edward C. Smith  
Professor

Department of Mechanical and Nuclear Engineering    Department of Aerospace Engineering  
The Pennsylvania State University, University Park, PA, USA

Conor Marr  
Manager, Mechanical Technology Development  
LORD Corporation  
Erie, PA, USA

## ABSTRACT

In order to reduce vibration, researchers have been exploring alternatives to conventional rigid pitch links. One viable passive vibration reduction device is the fluidic pitch link. By replacing rigid pitch links on rotorcraft with fluidic pitch links, changes can be made to the blade torsional impedance. At high frequencies, the pitch link impedance can be tuned to change the blade pitching response to higher harmonic loads. Although all have not been demonstrated simultaneously, fluidic pitch links have been shown to be able to reduce rotor power and all six hub forces and moments. A positive impact on aeroelastic stability from several fluidic pitch link designs has been shown for hover and forward flight. This paper will focus on validating the model that has been used in previous research via matching experimental and simulation results. A prototype fluidic pitch link has been designed, built, and tested at LORD Corporation. Displacement, load, and pressure were recorded during testing. Frequency and time response results were compared between simulation and experiment to validate the model. Three different fluid circuits were used, and the model was able to accurately predict performance for each of them with the exception of inaccuracy at low frequency due, in part, to the frequency dependence of the elastomer. An additional fourth circuit was tested that included a needle valve. The model did not accurately predict results across the entire range of valve positions, but the model was able to accurately match the dynamic stiffness amplitude using empirical parameters from a parameter study.

## 1. NOTATION

$A$	Piston cross-sectional area	$k_d$	Elastomer stiffness
$A_{FT}$	Fluid track cross-sectional area	$m_c$	Mass of the pitch link body
$C_b$	Bottom fluid chamber capacitance	$m_f$	Equivalent fluid mass
$c_d$	Elastomer damping	$m_p$	Mass of the piston
$c_f$	Equivalent fluid damping	$p_b$	Pressure in the top fluid chamber
$C_t$	Top fluid chamber capacitance	$p_t$	Pressure in the bottom fluid chamber
$D$	Fluid track inner diameter	$R$	Blade radius
$F$	Axial force on pitch link	$R_f$	Fluid resistance
$I$	Fluid inertance	$R_{fu}$	Uncorrected fluid resistance
$I_u$	Uncorrected fluid inertance	$r_0$	Fluid track inner radius
$L$	Fluid track length	$V$	Volume of fluid that enters the fluid track
$K_b$	Stiffness due to the bottom fluid chamber capacitance	$x$	Piston displacement
$K_t$	Stiffness due to the top fluid chamber capacitance	$z$	Displacement of fluid into the inertia track
$K^*$	Dynamic or complex stiffness	$\alpha$	Non-dimensional correction factor for calculating fluid resistance and inertance
$K'$	Real part of the dynamic stiffness	$\mu$	Dynamic viscosity
$K''$	Imaginary part of the dynamic stiffness	$\nu$	Kinematic viscosity
		$\rho$	Fluid density
		$\omega$	Frequency of oscillation
		$\Omega$	Rotor rotational speed

- $\overline{(\ )}$  Non-dimensional parameter  
 $(\ )^*$  Non-dimensional derivative

## 2. INTRODUCTION AND BACKGROUND

Researchers have been exploring alternatives to conventional rigid pitch links in order to reduce rotorcraft hub and pitch link vibration, increase pilot comfort, and extend component life. A pitch link is a rigid rod with spherical end bearings that connects the swashplate to the pitch horn, which is in turn connected to the blade root. An example of a conventional pitch link for a light duty helicopter with a hingeless rotor and axial bearings for pitch motion is pictured in Figure 1 to illustrate these connections. When the pilot moves the collective pitch lever, a static or 0/rev event, the swashplate moves vertically thus pitching all four blades equally and changing the thrust magnitude. When the pilot moves the cyclic pitch stick, a 1/rev event, the swashplate angles thus changing the thrust direction. Additionally, there are higher harmonic aerodynamic blade excitations at 2/rev and higher frequencies that load the pitch link. These excitations can lead to high pitch link loads, which can limit maximum forward speed and may pose fatigue and vibration challenges<sup>[1]</sup>.



Fig. 1: MBB Bo105 main rotor head and swashplate assembly. Adapted from ©1988 Burkhard Domke<sup>[2]</sup> and used with permission.

Milgram et al.<sup>[3]</sup> analyzed replacing conventional pitch links with a spring and damper element. The spring and damper element showed moderate improvements in hub loads. Han et al.,<sup>[4]</sup> inspired by the work of McGuire<sup>[5]</sup> that introduced Fluidlastic<sup>®</sup> dampers and isolators for vibration control in helicopters, explored using a Fluidlastic<sup>®</sup> isolator to reduce pitch link loads and were able to show a significant reduction in higher harmonic pitch link loads. Scarborough et al.<sup>[6]</sup> examined impedance tailoring fluidic pitch links (FPLs) for reduction of hub loads in high speed flight conditions. Using a rotor aeroelastic simulation, FPLs demonstrated the ability to influence all hub forces and moments as well as moderately decreasing rotor power required. Zhang et al.<sup>[7]</sup> added

a free wake model to the simulation in order to explore low forward speed. The results continue to show the potential for vibratory control. Treacy et al.<sup>[8]</sup> explored the aeroelastic stability of an articulated rotor with FPLs in hover and forward flight, which demonstrated the ability of FPLs to provide a stabilizing effect for the pitch mode in cases with high fluid resistance. Up to this point, research into FPLs had been purely simulation. This work focuses on experimentally validating a FPL model.

The prior FPL work examined a single pumper design. However, as noted by Vahdati<sup>[9]</sup>, double pumps are more commonly used in aerospace applications due to their increased safety and reduced risk of fluid cavitation. If the top elastomer fails in a double pumper design, the top and bottom plates will still remain rigidly connected as opposed to the single pumper design, which will separate, thus increasing the safety of the part. Additionally, since stiff elastomers are typically used in the top and bottom sections, double pumps are more easily pressurized than single pumps, which use a soft diaphragm in the lower chamber. This reduces the risk of cavitation in double pumper designs. Accordingly, the objective of this paper is to experimentally validate a double pumper FPL model.

## 3. FLUIDIC PITCH LINK MODELING

A schematic of a FPL is illustrated in Figure 2. There are two degrees of freedom: piston displacement,  $x$ , and volume of fluid displaced into the fluid track from equilibrium,  $V$ . The volume is not deterministic from the piston displacement due to the compressibility in the fluid and bulging of the elastomer. The elastomer sections act as parallel springs and dampers with axial stiffnesses,  $k_d/2$ , and damping coefficients,  $c_d/2$ , respectively. The top and bottom fluid chambers have capacitances  $C_t$  and  $C_b$ , respectively. The fluid track has cross-sectional area,  $A_{FT}$ ; fluid resistance,  $R_f$ ; and inertance,  $I$ . The inertance is defined as

$$(1) \quad I = \frac{\rho L}{A_{FT}},$$

where  $\rho$  is the fluid density and  $L$  is the fluid track length. The pitch link body has mass,  $m_c$ . The equations for the mechanical-fluidic coupling are

$$(2) \quad p_t = \frac{1}{C_t} [Ax - V]$$

and

$$(3) \quad p_b = \frac{1}{C_b} [V - Ax].$$

$A$  is the cross-sectional area of the piston. The equation for the fluid flow through the fluid track is

$$(4) \quad p_t - p_b = I\dot{V} + R_f\dot{V}.$$

Eqs. (2-3) can then be substituted into Eq. (4) in order to determine the first equation of motion,

$$(5) \quad I\ddot{V} + R_f\dot{V} + \left(\frac{1}{C_t} + \frac{1}{C_b}\right)V - A\left(\frac{1}{C_t} + \frac{1}{C_b}\right)x = 0.$$

The second equation of motion can be found by summing the forces on the piston,

$$(6) \quad m_p\ddot{x} + c_d\dot{x} + \left[A^2\left(\frac{1}{C_t} + \frac{1}{C_b}\right) + k_d\right]x - A\left(\frac{1}{C_t} + \frac{1}{C_b}\right)V = F.$$

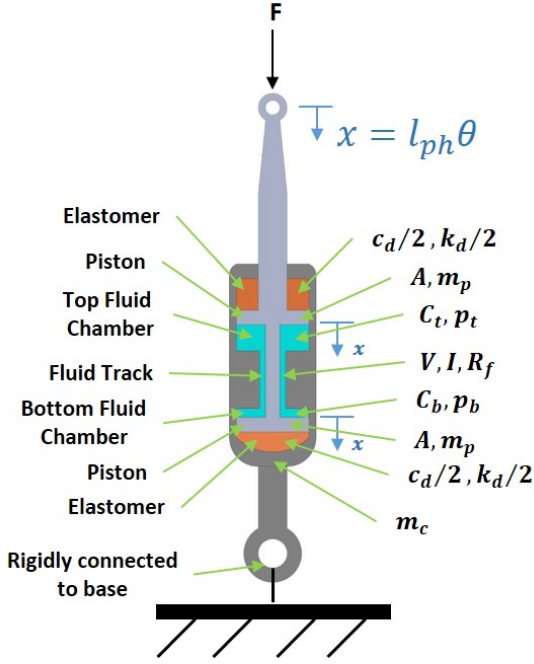


Fig. 2: Model of a double pumper fluidic pitch link.

Additionally, the equivalent mechanical model of this system can be derived and is illustrated in Figure 3. The vertical displacement of the fluid in the fluid track,  $z$ , is related to the volume of fluid displaced from equilibrium,  $V$ , by

$$(7) \quad z = \frac{V}{A_{FT}}.$$

The fluid resistance,  $R_f$ , can be represented by a damper,  $c_f$ , where

$$(8) \quad c_f = R_f A_{FT}^2.$$

The inertance,  $I$ , can be represented by a mass,  $m_f$ , where

$$(9) \quad m_f = I A_{FT}^2.$$

The capacitances in the top and bottom chambers,  $C_t$  and  $C_b$ , respectively, can be treated as springs related to the piston area by

$$(10) \quad K_t = \frac{A^2}{C_t}$$

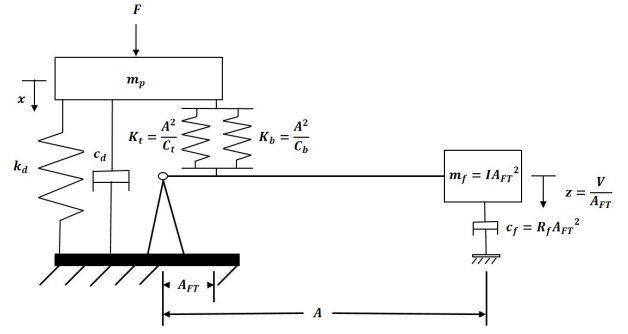


Fig. 3: Mechanical model of a double pumper fluidic pitch link.

and

$$(11) \quad K_b = \frac{A^2}{C_b}.$$

### 3.1. Nondimensionalization

The non-dimensionalization scheme follows from the work completed in Treacy et al.<sup>[8]</sup> Multiply Eq. 5 by  $R^2$  where  $R$  is a rotor radius. Then divide the resulting equation and Eq. 6 by  $m_b\Omega^2R^2$  to obtain

$$(12) \quad \begin{bmatrix} \bar{I} & 0 \\ 0 & \bar{m}_p \end{bmatrix} \begin{bmatrix} \bar{V} \\ \bar{x} \end{bmatrix} + \begin{bmatrix} \bar{R}_f & 0 \\ 0 & \bar{c}_d \end{bmatrix} \begin{bmatrix} \dot{\bar{V}} \\ \dot{\bar{x}} \end{bmatrix} + \begin{bmatrix} \bar{k}_1 & -\bar{k}_{12} \\ -\bar{k}_{12} & \bar{k}_2 \end{bmatrix} \begin{bmatrix} \bar{V} \\ \bar{x} \end{bmatrix} = \begin{bmatrix} 0 \\ \bar{F} \end{bmatrix}.$$

The bars indicate a non-dimensionalized parameter. The mass per unit span of a rotor blade is  $m_b$  while  $\Omega$  is the blade rotation frequency. Note that  $m_p$  is a mass while  $m_b$  is a mass per unit length. The piston displacement,  $x$ , and volume of fluid displaced from equilibrium in the fluid track,  $V$ , are non-dimensionalized by  $R$  and  $R^3$ , respectively, such that

$$(13) \quad \bar{x} = \frac{x}{R},$$

$$(14) \quad \bar{V} = \frac{V}{R^3}.$$

The non-dimensional derivatives are given by

$$(15) \quad \dot{(\quad)}^* = \frac{(\quad)}{\Omega}.$$

All of the non-dimensional parameters are given in the Appendix as Eqs. (A.1–A.12).

## 4. TEST SETUP

A FPL was designed, manufactured, and tested at LORD Corporation in order to obtain the veracity of the FPL model. In particular, a new swappable fluid track design has been created to allow multiple track lengths to be tested. Please keep in mind that the external fluid track is for prototype purposes to enable flexibility in circuit design for interchanging the fluid track. A typical production level design makes use of an internal fluid track. However, an external fluid track has been demonstrated in a LIVE pylon mount for the Bell 505 Jet Ranger X<sup>[10]</sup> and could be integrated into a production level design if it were beneficial to the performance or design of a FPL. Four circuits were tested and CAD models of each are illustrated in Figures 4–5. An additional feature of this model, two pressure transducers are attached to obtain the pressure difference between the top and bottom fluid chambers. A cross-section of the CAD model with components labeled is illustrated in Figure 6.

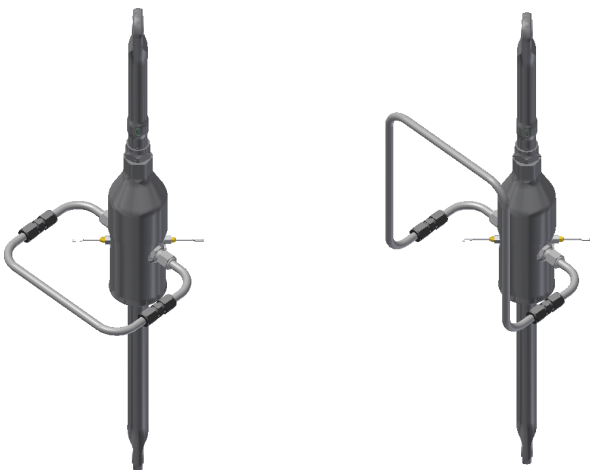


Fig. 4: CAD models of fluidic pitch links with circuit 1 (left) and circuit 2 (right).

A CAD model of the fluid track design with circuit 1 attached is illustrated in Figure 7. The top and bottom faces of this part contact the fluid in the top and bottom chambers of the fluidic pitch link. Large slots on the top and bottom faces have been milled to minimize the resistance of the fluid flow through the fluid track. SAE o-ring bosses enable fluid to flow radially into and out of the part. These features are illustrated in the CAD models shown in Figures 8–9. A Parker Ferulok<sup>®</sup> adapter is used to connect the SAE port to the tubing via compression fitting. An adapter connects the pressure transducers to the machined slots in order to record the pressure in the two fluid chambers. After a 90° bend, a union with compression fittings on both ends enables swapping of the tubing to

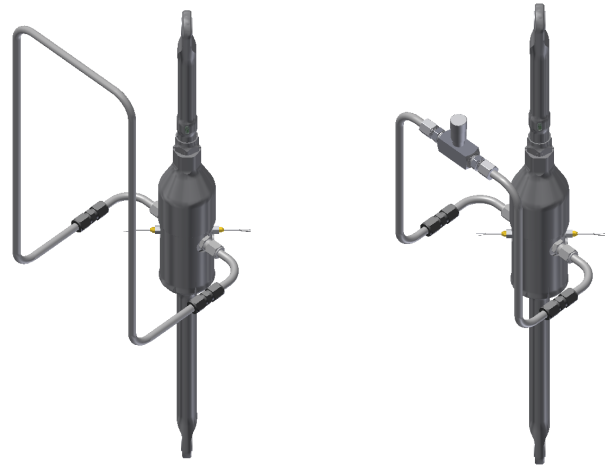


Fig. 5: CAD models of fluidic pitch links with circuit 3 (left) and circuit 4 (right).

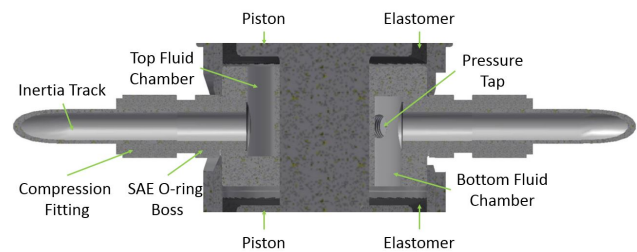


Fig. 6: CAD model of a fluidic pitch link cross-section.

test the varying tubing lengths.

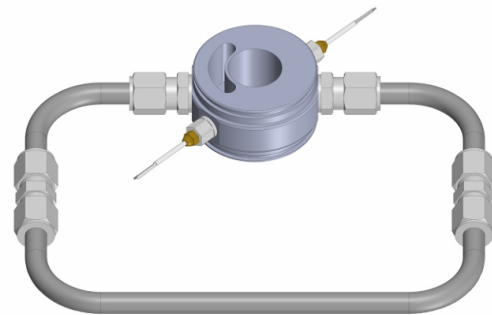


Fig. 7: CAD model of the fluid track with circuit 1.

Systematic tubing length changes between circuits 1-3 provide three different inertance values, which shift the natural frequencies of the system. The fourth circuit (Figure 5b) has an additional needle valve component. The needle valve was used to increase the resistance, which reduces the amplitudes at the notch

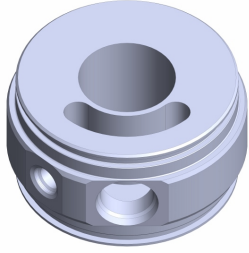


Fig. 8: CAD model of fluid track without circuitry attached.

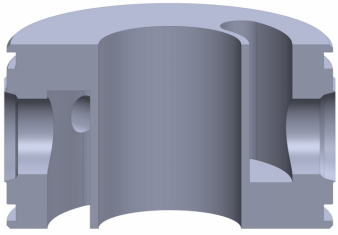


Fig. 9: CAD model of fluid track cross-section without circuitry attached.

and peak frequencies.

Each of the four circuit designs was tested at LORD Corporation in an MTS single-axis test machine as pictured in Figure 10. The bottom of the fluidic pitch link is fixed while the top can be hydraulically displaced to meet given force or displacement criteria. For a dynamic stiffness test, the fluidic pitch link is cycled for ten seconds at a given frequency and displacement amplitude and data is recorded during the final four seconds. The recorded force amplitude and displacement amplitude are then used to calculate the dynamic stiffness. During testing, in addition to recording force, displacement, and stiffness, the pressures in each chamber were recorded. The frequency sweep for each circuit was conducted by successively increasing frequency until the notch was captured.

## 5. ANALYSIS METHODOLOGY

Two analysis methods were used for successfully validating the FPL model. The first method applied FPL design parameters to a simulation for comparison of our model with recorded experimental data in the time-domain and frequency-domain. This method was conducted when simulating circuits 1-3. The objective of this method was to evaluate the validity of the model to predict the experimental results. The second method utilized an empirical parameter study

to match the time-domain and frequency-domain data from testing via simulation results. This method was employed for the valve closing study using circuit 4. The objective of this method was to evaluate the validity of the model to match the experimental results if the first method failed and to make note of any missing dynamics.



Fig. 10: MTS single axis test at LORD Corp.

The empirical FPL parameters were obtained by performing a brute force parameter study and minimizing the  $l^2$ -norm<sup>[11]</sup> of the error between the simulation and experimental results, which is equal to

$$(16) \quad \|e\|_{l^2} = \sqrt{\sum_{k=1}^n (u_k^s - u_k^t)^2},$$

where  $u$  represents a vector of any frequency-dependent or time-dependent variable. The superscripts  $s$  and  $t$  denote simulation and experiment, respectively. A parameter study was initiated by altering six FPL parameters and then calculating the  $l^2$ -norm of the error for the frequency response of the dynamic stiffness amplitude at the discrete test frequencies. The piston area,  $A$ ; capacitance in the top chamber,  $C_t$ ; capacitance in the bottom chamber,  $C_b$ ; fluid resistance,  $R_f$ ; elastomer stiffness,  $k_d$ ; and inductance,  $I$ , were varied in order to obtain the minimum error. It was assumed that the two capacitances are equal since they derive from the same component. However, due to allowable tolerances, they are slightly different from their nominal design value, which is expounded in the results section.

In order to simulate the model, a standard state-space representation is created in MATLAB using the function “ss.m” and the equations of motion in

first order form. There is zero feedforward. The outputs are pressure in the top chamber,  $p_t$ ; pressure in the bottom chamber,  $p_b$ ; and displacement of the piston,  $x$ . The recorded force data from the experiment was used as an input to the MATLAB function "lsim.m" to calculate the time response. The frequency response was calculated by using the MATLAB function "bode.m" with the specified frequency vector from the corresponding circuit. To obtain the dynamic stiffness results, the amplitude from the transfer function with an input of  $\bar{F}$  and output of  $\bar{x}$  was inverted and the phase angle was negated. Thus the dynamic stiffness is defined as

$$(17) \quad \bar{K}^* = \frac{\bar{x}}{\bar{F}} = \bar{K}' + j\bar{K}'' ,$$

where  $j = \sqrt{-1}$  is the imaginary unit.  $\bar{K}'$  is the real part of the dynamic stiffness and is a measure of the FPL's stiffness.  $\bar{K}''$  is the imaginary part of the dynamic stiffness and is a measure of the FPL's damping.

Two of the FPL parameters are frequency dependent: fluid resistance,  $R_f$ , and inertance,  $I$ . These parameters are calculated at each frequency using the manner recommended by Donovan et al<sup>[12]</sup>. The equation for fluid resistance is a modification to the resistance from Poiseuille flow and, in the frequency range of interest, is equal to

$$(18) \quad R_f = \frac{128\mu L}{\pi D^4} 0.166\alpha^{1.49}, \alpha > 10,$$

where  $\mu$  is the fluid dynamic viscosity and  $D$  is the tube inner diameter.  $\alpha$  is a non-dimensional parameter that is a function of the frequency of oscillation,  $\omega$ . The equation for  $\alpha$  is

$$(19) \quad \alpha = r_0 \sqrt{\frac{\omega}{\nu}},$$

where  $r_0$  is the tube inner radius and  $\nu$  is the fluid kinematic viscosity. Inertance is modified by multiplying Eq. 1 by a correction factor that is obtained from a look-up table when  $\alpha$  is an input.

Frequency responses from the experimental results were generated by applying a discrete Fourier transform (DFT) to the time response data at each frequency using the MATLAB function "fft.m" to obtain the complex Fourier coefficients. The magnitude and phase can then be obtained from these coefficients by taking the absolute value and finding the angle between the real and imaginary parts, respectively. In order to obtain the correct magnitude amplitudes for a single-sided amplitude spectrum, the coefficients were normalized by the length of the signal and then non-zero frequency components were multiplied by two.

## 6. RESULTS

Results are presented in a unique manner for each circuit to best demonstrate the multitude of comparisons that can be made. For each of circuits 1-3, frequency spectrums are reported for dynamic stiffness amplitude and the amplitude of the pressure divided by force. The results for circuit 1 additionally contain phase phase data for the frequency spectrums, the real part of the dynamic stiffness, and the complex part of the dynamic stiffness. The results for circuit 2 additionally includes time-responses of displacement and the pressure in each chamber at a given frequency. The results for circuit 3 additionally incorporate displacement and pressure plotted against force at various frequencies. These plots are similar to Lissajous figures<sup>[13]</sup>. Lissajous figures are a special case of parametric equations where  $x$ - and  $y$ - coordinates are written as

$$(20) \quad x = x_0 \sin(\omega_x t + \phi_x),$$

and

$$(21) \quad y = y_0 \sin(\omega_y t + \phi_y).$$

DFTs were then applied to the force, displacement, and pressure at the individual test frequencies to evaluate the effects of the magnitudes and phases from the first three harmonics. The dynamic stiffness amplitude is presented for the valve closing study at numerous valve positions to explore the effect of closing the valve on the dynamic stiffness amplitude.

The FPL parameters that were unaffected by circuit alterations and used in the simulations for circuits 1-3 are enumerated in Table 1

Table 1: Fluidic Pitch Link Properties for Circuits 1-3

Property	Value
$\bar{k}_d$	66.95
$\bar{A}$	$5.103 \times 10^{-5}$
$\bar{c}_d$	$8.048 \times 10^{-2}$
$\bar{C}_t$	$5.267 \times 10^{-13}$
$\bar{C}_b$	$5.267 \times 10^{-13}$
$\bar{m}_p$	$5.814 \times 10^{-3}$
$\bar{k}_1$	$1.151 \times 10^{11}$
$\bar{k}_2$	366.6
$\bar{k}_{12}$	$5.872 \times 10^6$

### 6.1. Circuit 1

The non-dimensional uncorrected fluid resistance,  $\bar{R}_{fu}$ , is  $4.237 \times 10^6$ . For the remainder of the paper, all parameters are assumed to be non-dimensional

unless otherwise stated. The uncorrected inertance,  $\bar{I}_u$ , is  $4.555 \times 10^8$  as defined in dimensional form in Eq. 1. The equation for the dimensional uncorrected fluid resistance is

$$(22) \quad R_{fu} = \frac{128\mu L}{\pi D^4}.$$

The dynamic stiffness amplitude and phase frequency spectra for circuit 1 are presented in Figure 11. For all of the frequency responses, the solid red line is the simulation result while the blue triangles denote discrete test points. The simulation result accurately replicates the depth and location of the notch frequency. In the simulation, the notch frequency occurs at 6.8/rev while the experimental results represent the notch at approximately 6.67/rev, which is less than 2% error. However, the model break downs at low frequency due in part to a frequency dependence of the elastomer that is unmodeled. This frequency dependence can further be observed in the real and imaginary parts of the dynamic stiffness, which are illustrated in Figure 12 and Figure 13, respectively. The real part of the dynamic stiffness shows the frequency dependence of the stiffness at low frequency. Additionally, negative stiffness that is observed in the real part of the dynamic stiffness after the notch frequency can be attributed to the phase shift that is illustrated in Figure 11b as the frequency increases. The imaginary part of the dynamic stiffness, which is a measurement of the damping in the system, reveals an even greater dependence on frequency both at low frequency due to the elastomer and throughout the frequency range due to the frequency dependence of the fluid resistance. The correction to the resistance formula is able to capture the curvature of the line, which would be straight for a constant coefficient resistance. However, the low frequency elastomer dependence is even more apparent as there is a large shift in the damping that gives the appearance of non-zero static damping even though the curve for the experiment will tend to zero if tested at small enough frequencies.

The pressure divided by force amplitude and phase frequency spectra are reported in Figure 14 and Figure 15 for the top and bottom fluid chambers, respectively. The phase has been wrapped to  $\pm 180^\circ$  for clarity. The amplitudes in both chambers match well; however, the amplitude of the pressure in each chamber differs slightly due to the variability of the capacitances in each tubeform from acceptable component tolerances that can be accounted for in the model by enabling  $C_t \neq C_b$ . However, this was not accounted for in this simulation since the tubeform nominal values are the same. While the amplitudes of the pressures in each chamber nearly match, the phase between each chamber varies by  $180^\circ$  as is expected from Eqs. 2–3, which shows that the pressures should be equal and opposite for  $C_t = C_b$ .

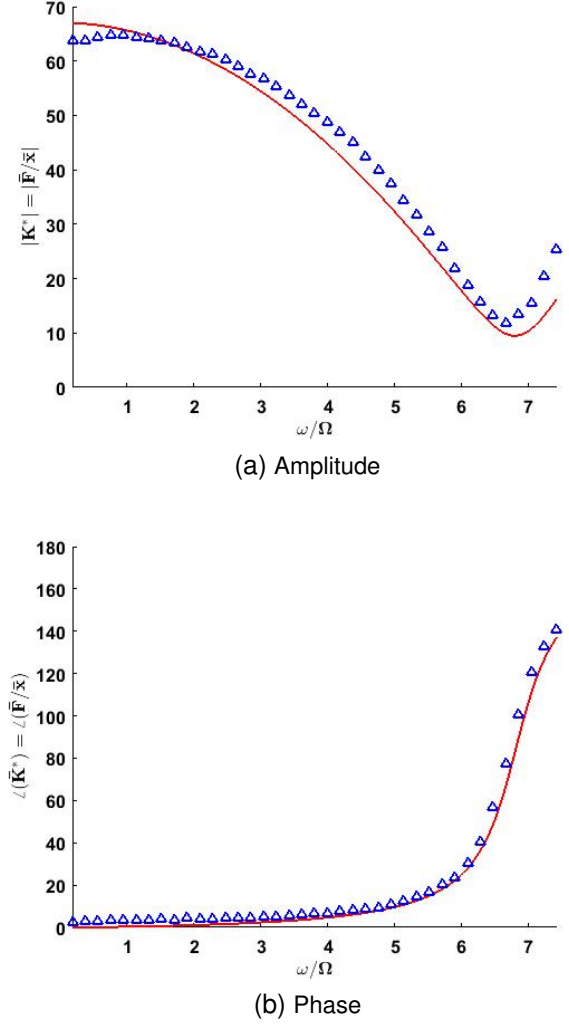


Fig. 11: Dynamic stiffness (a) amplitude and (b) phase of circuit 1. The simulation result is the red line while the experimental results are blue triangles.

## 6.2. Circuit 2

The uncorrected fluid resistance,  $\bar{R}_{fu}$ , is  $8.901 \times 10^6$  and the uncorrected inertance,  $\bar{I}_u$ , is  $9.570 \times 10^8$ . The frequency spectrum for the dynamic stiffness amplitude is illustrated in Figure 16. With the longer fluid track, both resistance and inertance increase. Accordingly, the notch frequency shifts left and contains a slightly shallower valley than in circuit 1. The experimental notch frequency is approximately 4.85/rev while the simulation predicts that the notch frequency will occur at 4.68/rev. The error in the notch frequency location is slightly greater than in circuit 1, but it is still very good at 3.5%. Frequency spectra for the amplitudes of the pressures divided by force are illustrated in Figure 17 and Figure 18 for the top and bottom fluid chambers, respectively. The amplitude is predicted very well when accounting for the inaccuracy in the notch frequency.

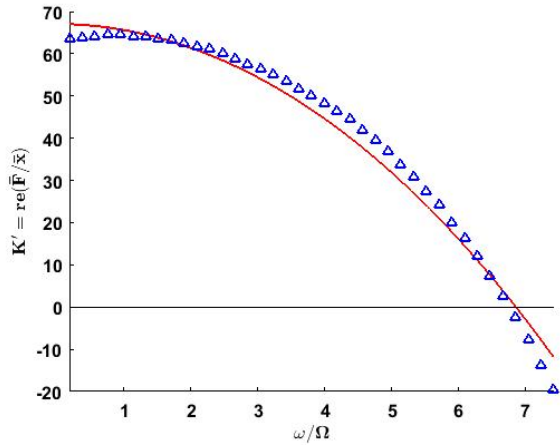


Fig. 12: Real component of the dynamic stiffness of circuit 1. The simulation result is the red line while the experimental results are blue triangles.

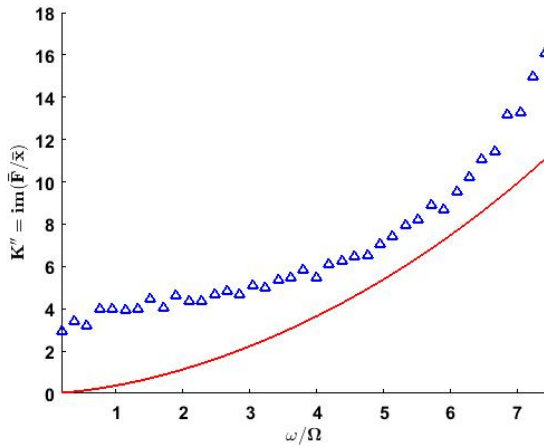
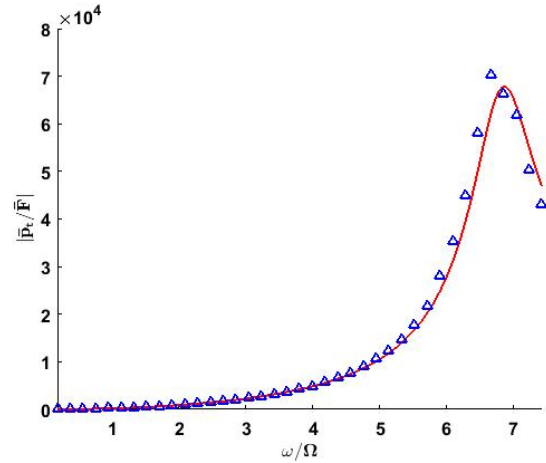
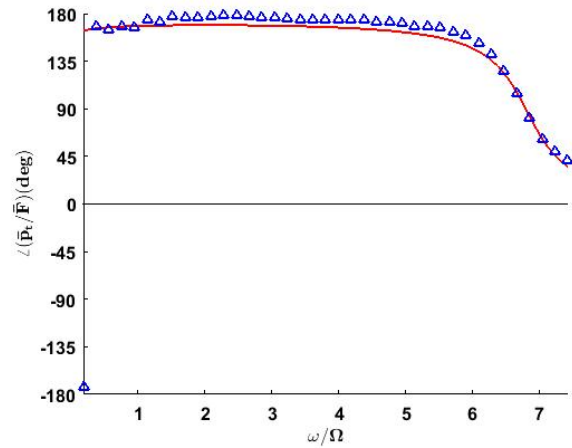


Fig. 13: Imaginary component of the dynamic stiffness of circuit 1. The simulation result is the red line while the experimental results are blue triangles.

As expected from the dynamic stiffness frequency response, the simulation and experimental results of the time response of the position at 0.95/rev, which is presented in Figure 19, match exceptionally well. The time response of the pressure in the top chamber at 3.81/rev is illustrated in Figure 20. The simulation overpredicts the peak pressure by 26%, which is to be expected from viewing the corresponding amplitude in the frequency spectrum from Figure 17. The time response of the pressure in the bottom chamber at 5.52/rev is illustrated in Figure 21. The simulation underpredicts the peak pressure by 8% and can similarly be expected by viewing the corresponding frequency spectrum.



(a) Amplitude

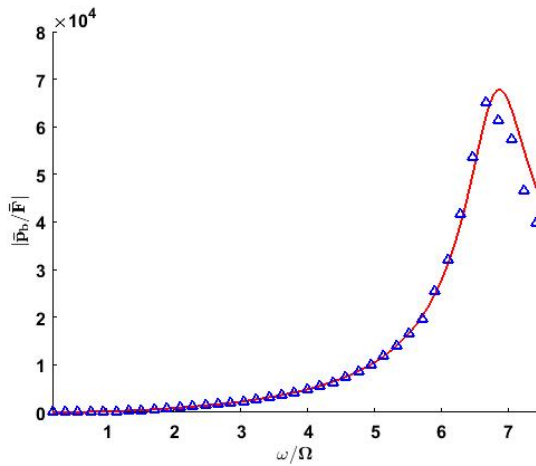


(b) Phase

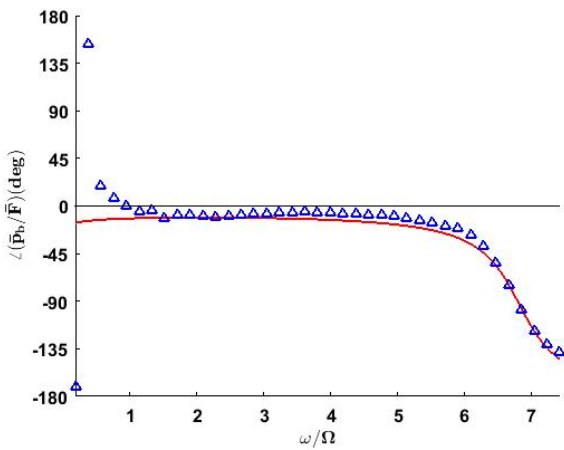
Fig. 14: (a) Amplitude and (b) phase frequency response of pressure in the top chamber divided by force for circuit 1. The simulation result is the red line while the experimental results are the blue triangles.

### 6.3. Circuit 3

The uncorrected fluid resistance,  $\bar{R}_{fu}$ , is  $1.357 \times 10^7$  and the uncorrected inertia,  $\bar{I}_u$ , is  $1.459 \times 10^9$ . The frequency spectrum for the dynamic stiffness amplitude is illustrated in Figure 22. The longer fluid track will again cause both resistance and inertia to increase and thus the notch frequency further shifts left and contains a slightly shallower valley in comparison with the previous two circuits. The experimental notch frequency is approximately 4.1/rev while the simulation predicts that the notch frequency will occur at 3.78/rev. The error in the notch frequency seems to be trending up with the longer fluid tracks as it reaches 7.8% for circuit 3. The frequency spectrum for the amplitude of the pressure in the top chamber divided by force is illustrated in Figure 23. The amplitude is again predicted very well when accounting for



(a) Amplitude



(b) Phase

Fig. 15: (a) Amplitude and (b) phase frequency response of pressure in the bottom chamber divided by force for circuit 1. The simulation result is the red line while the experimental results are the blue triangles.

the inaccuracy in the notch frequency.

Force versus position at 3.62/rev is illustrated in Figure 24. The simulation is able to accurately predict the shape of the curve, but it overpredicts the displacement amplitude. The bow tie shape occurs when the vertical axis frequency is double the frequency of the horizontal axis and the phase difference is a multiple of  $90^\circ$ . The amplitudes and phases for the first three harmonics of the input frequency are illustrated in Figure 25 and Figure 26 for the force input and displacement results, respectively. The force input has the largest amplitude at the second harmonic, but it also has significant amplitudes at the first and third harmonics. The displacement results show a dominating peak in the amplitude at the input frequency. The phases at the second harmonic of the force input and the first harmonic of the displacement are both close to  $-90^\circ$ . Thus Figure 24 has the bow tie shape

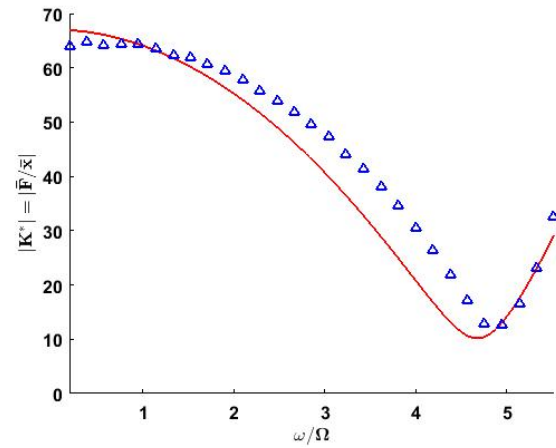


Fig. 16: Dynamic stiffness amplitude of circuit 2. The simulation result is the red line while the experimental results are blue triangles.

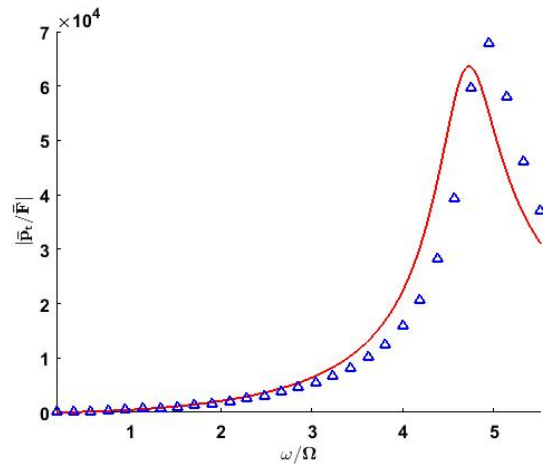


Fig. 17: Amplitude of the pressure in the top chamber divided by force for circuit 2. The simulation result is the red line while the experimental results are blue triangles.

due to the dominant force amplitude having double the frequency of the dominant displacement amplitude and zero phase shift. The amplitudes from the other harmonics cause skewing of the bow tie.

The corresponding pressure in the top chamber versus force plot at 3.81/rev is illustrated in Figure 27. Similar to the force versus displacement curve, the simulation is able to accurately predict the shape of the curve, but it overpredicts the pressure amplitude. The amplitude and phase for the first three harmonics of the pressure are illustrated in Figure 28. There are large pressure amplitudes at the first two harmonics that are equal in size. The phase is close to  $90^\circ$  for the first harmonic and  $-90^\circ$  for the second harmonic. A  $45^\circ$  degree line occurs when the frequencies between the horizontal and vertical axes are equal and

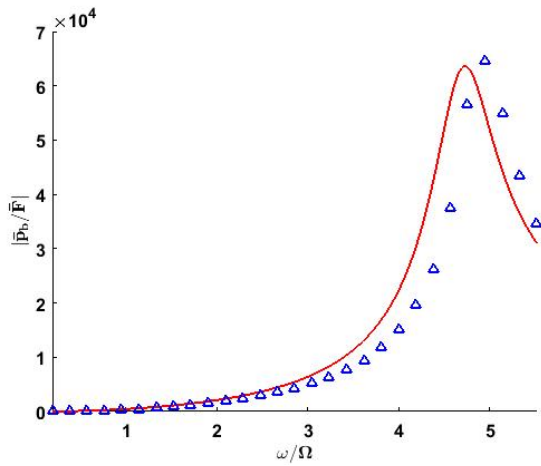


Fig. 18: Amplitude of the pressure in the bottom chamber divided by force for circuit 2. The simulation result is the red line while the experimental results are blue triangles.

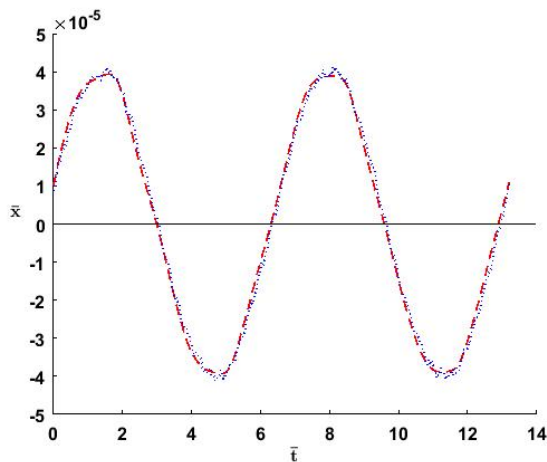


Fig. 19: Position versus time of circuit 2 at 0.95/rev for two cycles. The simulation result is the red dashed line while the experimental result is the blue dotted line.

the phases are separated by a multiple of  $180^\circ$ . Thus the pressure in the top chamber versus force plot is a combination of a  $45^\circ$  degree line due to amplitudes from the pressure and force at the second harmonic with zero phase shift and a vertical bow tie due to the pressure amplitude at the first harmonic and the force amplitude at the second harmonic with a  $180^\circ$  phase shift.

#### 6.4. Circuit 4 Valve Closing Study

The dynamic stiffness amplitudes for multiple valves positions are illustrated in Figure 29. The model was unable to accurately predict the response when the FPL design parameters were input, so an empirical

parameter study with constant coefficients was used to minimize the error in order to match the dynamic stiffness at each of the valve positions. The model predictions and experiment were set up with the expectation that the notch frequency for the fully open valve would be similar to the notch frequency from circuit 2 ( $\sim 4.8/\text{rev}$ ). However, the figure shows that the notch frequency is actually approximately  $3.8/\text{rev}$ . Using the method established in Section 5, the simulation is able to accurately match the experiment at each valve position. The values of each parameter that minimized the dynamic stiffness for each valve position are enumerated in Table 2.

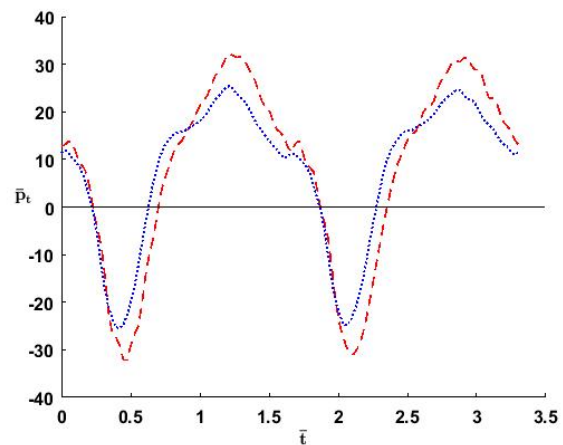


Fig. 20: Pressure in the top chamber versus time of circuit 2 at 3.81/rev for two cycles. The simulation result is the red dashed line while the experimental result is the blue dotted line.

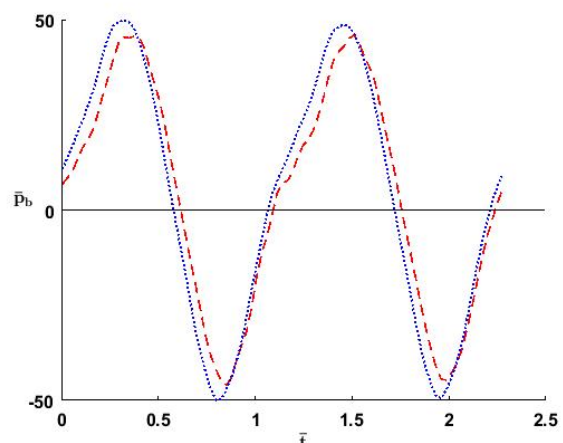


Fig. 21: Pressure in the bottom chamber versus time of circuit 2 at 5.52/rev for two cycles. The simulation result is the red dashed line while the experimental result is the blue dotted line.

Table 2: Fluidic Pitch Link Properties for Valve Closing Study

Property	Fully Open	3 Turns Closed	5 Turns Closed	7 Turns Closed	Fully Closed
$\bar{I}$	$1.301 \times 10^9$	$1.858 \times 10^9$	$1.858 \times 10^9$	$1.858 \times 10^9$	$1.114 \times 10^9$
$\bar{R}_f$	$1.349 \times 10^9$	$2.575 \times 10^9$	$1.839 \times 10^{11}$	$7.970 \times 10^{10}$	$1.594 \times 10^{11}$
$\bar{k}_d$	66.78	66.78	63.27	59.75	98.41
$\bar{A}$	$3.945 \times 10^{-5}$	$3.945 \times 10^{-5}$	$6.136 \times 10^{-5}$	$2.191 \times 10^{-5}$	$2.191 \times 10^{-5}$
$\bar{c}_d$	$8.048 \times 10^{-2}$	$8.048 \times 10^{-2}$	$8.048 \times 10^{-2}$	$8.048 \times 10^{-2}$	$8.048 \times 10^{-2}$
$\bar{C}_t$	$1.483 \times 10^{-12}$	$1.483 \times 10^{-12}$	$1.032 \times 10^{-8}$	$5.547 \times 10^{-13}$	$5.547 \times 10^{-13}$
$\bar{C}_b$	$1.483 \times 10^{-12}$	$1.483 \times 10^{-12}$	$1.032 \times 10^{-8}$	$5.547 \times 10^{-13}$	$5.547 \times 10^{-13}$
$\bar{m}_p$	$5.814 \times 10^{-3}$	$5.814 \times 10^{-3}$	$5.814 \times 10^{-3}$	$5.814 \times 10^{-3}$	$5.814 \times 10^{-3}$
$\bar{k}_1$	$4.088 \times 10^{10}$	$4.088 \times 10^{10}$	$5.872 \times 10^6$	$1.093 \times 10^{11}$	$1.093 \times 10^{11}$
$\bar{k}_2$	130.4	130.4	63.29	112.2	150.9
$\bar{k}_{12}$	$1.613 \times 10^6$	$1.613 \times 10^6$	360.3	$2.394 \times 10^6$	$2.394 \times 10^6$

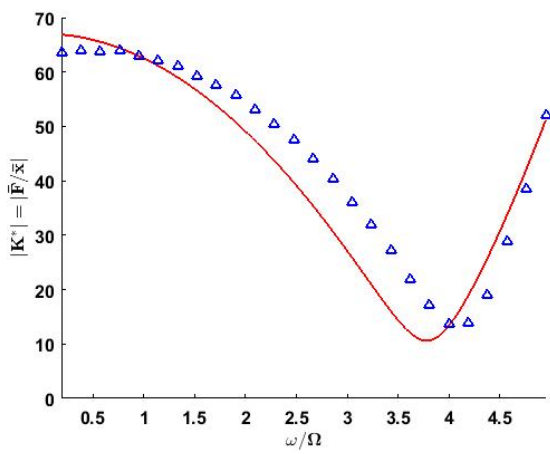


Fig. 22: Dynamic stiffness amplitude of circuit 3. The simulation result is the red line while the experimental results are blue triangles.

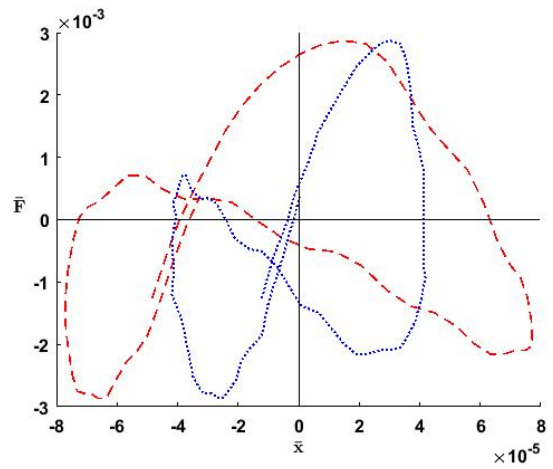


Fig. 24: Force versus position of circuit 3 at 3.62/rev for one cycle. The simulation result is the red dashed line while the experimental result is the blue dotted line.

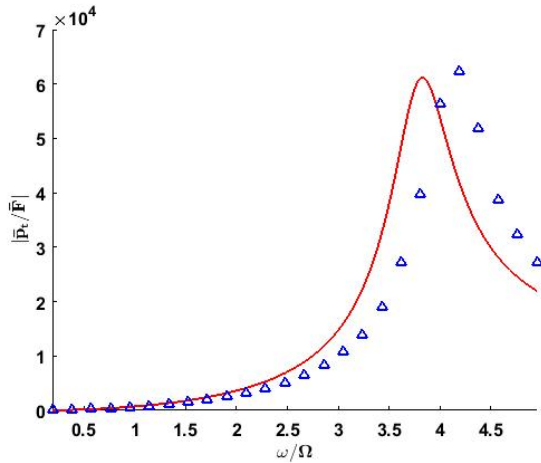


Fig. 23: Amplitude of the pressure in the top chamber divided by force for circuit 3. The simulation result is the red line while the experimental results are blue triangles.

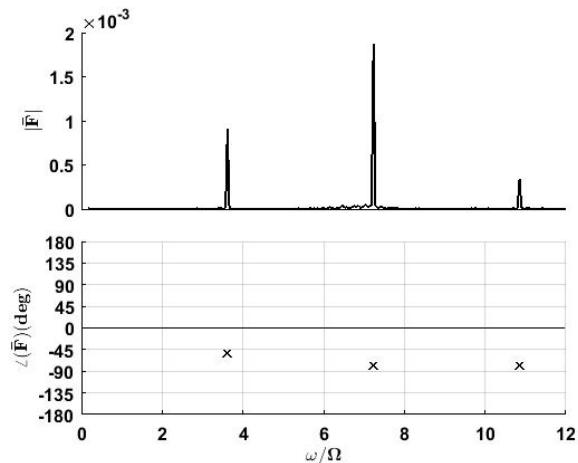


Fig. 25: Force magnitude and phase of circuit 3 at 3.62/rev. The black color indicates that force is the input.

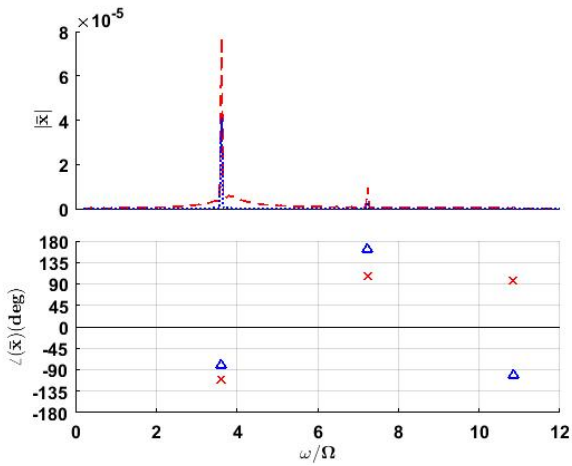


Fig. 26: Position magnitude and phase of circuit 3 at 3.62/rev. The simulation result is the red dashed line in the magnitude plot and a red x in the phase plot while the experimental result is the blue dotted line in the magnitude plot and a blue triangle in the phase plot.

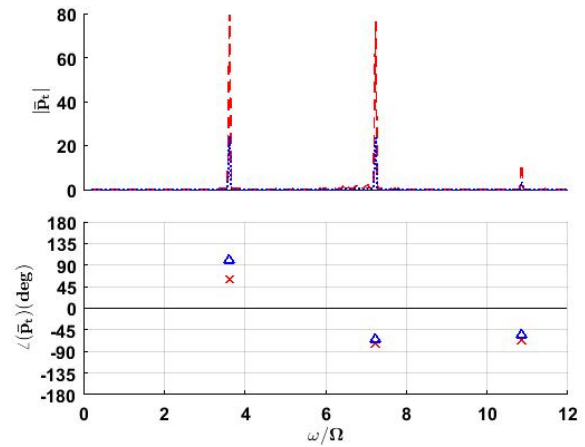


Fig. 28: Pressure in the top chamber magnitude and phase for circuit 3 at 3.62/rev. The simulation result is the red dashed line in the magnitude plot and a red x in the phase plot while the experimental result is the blue dotted line in the magnitude plot and a blue triangle in the phase plot.

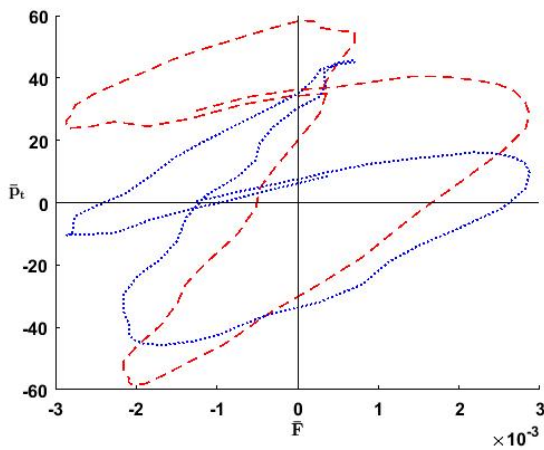


Fig. 27: Pressure in the upper chamber versus force of circuit 3 at 3.62/rev for one cycle. The simulation result is the red dashed line while the experimental result is the blue dotted line.

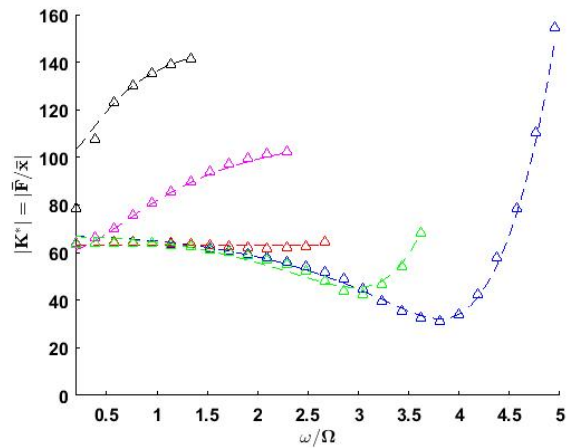


Fig. 29: Dynamic stiffness amplitude for multiple valve positions. The simulation results are dashed lines while the experimental results are triangles. Blue is fully open, green is three turns closed, red is five turns closed, magenta is seven turns closed, and black is fully closed.

## 7. CONCLUSIONS

1. The fluidic pitch link model is able to accurately capture the shape and depth of the notch for the dynamic stiffness frequency response and for the peak in the pressure frequency responses for circuits 1-3.
2. The location accuracy of the notch frequency varies with increasing fluid track length. As fluid track length increased, so did the error. For circuit 1, the shortest track length, the error in the notch frequency was less than 2% (.13/rev). For circuit 2, the medium track length, it was 3.5% (.17/rev). For circuit 3, the longest track length, it was 7.8% (0.32/rev). Local cavitation is a known issue that is unmodeled and may be a primary factor in altering the notch frequency from the predicted value to the experimental value.
3. The impact of the correction factors for the frequency dependent fluid resistance and inertia is significant and important when predicting FPL performance.
4. There are unmodeled dynamics at low frequencies largely due to the frequency dependence of the elastomer.
5. The model does not accurately predict the dynamic stiffness amplitude of the fluidic pitch link when there is a valve introduced into the fluid track as in the valve closing study performed using circuit 4. However, the model is capable of matching the dynamic stiffness when tuned empirically even when using constant coefficients for the FPL parameters. The predicted model drastically overstates the notch frequency, even for the fully open case, which was expected to be similar to the results of circuit 2. The softening may be due to local cavitation or eddies that could be forming near the valve.
6. Some of the errors in the model are likely to be attributed to the simplicity of the model. To improve the understanding of the flow through the inertia track and near the needle valve and to model those features better, a computational fluid dynamics analysis would be beneficial.

## ACKNOWLEDGMENTS

The authors would like to express their appreciation for the financial and technical support provided by LORD Corporation.

## REFERENCES

- [1] Kufeld, R. M. and Bousman, W. G., "High Load Conditions Measured on a UH-60A in Maneuver-

ing Flight," *Journal of the American Helicopter Society*, Vol. 43, (3), 1998, pp. 202–211.

- [2] ©Burkhard Domke, "Main Rotor Head and Swashplate Assembly." [Online; accessed June 28, 2017], 1988.
- [3] Milgram, J., Chopra, I., and Kottapalli, S., "Dynamically Tuned Blade Pitch Links for Vibration Reduction," Proceedings of the 50th American Helicopter Society Annual Forum, Washington, DC, May 11–13, 1994.
- [4] Han, D., Rahn, C. D., and Smith, E. C., "Higher Harmonic Pitch Link Loads Reduction using Fluidlastic Isolators," Proceedings of the Institution of Mechanical Engineers, Part G: Journal of Aerospace Engineering, March 2014.
- [5] McGuire, D. P., "Fluidlastic Dampers and Isolators for Vibration Control in Helicopters," Proceedings of the 50th American Helicopter Society Annual Forum, Washington, DC, May 11–13, 1994.
- [6] Scarborough, L. H., III, Rahn, C. D., Smith, E. C., Koudela, K. L., and Jolly, M. R., "Impedance Tailored Fluidic Pitch Links for Passive Hub Vibration Control and Improved Rotor Efficiency," Proceedings of the Fifth Decennial AHS Aeromechanics Specialists' Conference, San Francisco, CA, January 22–24, 2014.
- [7] Zhang, J., Scarborough, L. H., III, Smith, E. C., Rahn, C. D., and Jolly, M. R., "Evaluation of Fluidic Pitch Links for Rotor Hub Vibration Controls," Proceedings of the 40th European Rotorcraft Forum, Southampton, England, September 2–5, 2014.
- [8] Treacy, S. M., Rahn, C. D., Smith, E. C., and Marr, C., "Pitch-Flap Stability of an Articulated Rotor with Fluidic Pitch Links," Proceedings of the 2016 AHS Technical Meeting on Aeromechanics Design for Vertical Lift, San Francisco, CA, January 20–22, 2016.
- [9] Vahdati, N., "A Detailed Mechanical Model of a Double Pumper Fluid Mount," *Journal of Vibration and Acoustics*, Vol. 120, (2), 1998, pp. 361–370.
- [10] Romano, P. Q., Seifert, M., and Smith, M., "The 505 Low Vibration Solution," Proceedings of the 73rd American Helicopter Society Annual Forum, Fort Worth, TX, May 9–11, 2017.
- [11] Horn, R. A. and Johnson, C. R., *Matrix Analysis*, Cambridge University Press, New York, NY, 1990, Chapter 10, pp. 313–386.

- [12] Donovan, F., Taylor, B. C., and Su, M., "One-Dimensional Computer Analysis of Oscillatory Flow in Rigid Tubes," *Journal of Biomechanical Engineering*, Vol. 113, (4), 1991, pp. 476–484.
- [13] De Silva, C. W., *Vibration and Shock Handbook*, CRC Press, 2005.

## APPENDIX

$$(A.1) \quad \bar{I} = \frac{IR^3}{m_b}$$

$$(A.2) \quad \bar{m}_p = \frac{m_p}{m_b R}$$

$$(A.3) \quad \bar{R}_f = \frac{R^3 R_f}{m_b \Omega}$$

$$(A.4) \quad \bar{c}_d = \frac{c_d}{m_b \Omega R}$$

$$(A.5) \quad \bar{k}_1 = \frac{R^3 \left( \frac{1}{C_t} + \frac{1}{C_b} \right)}{m_b \Omega^2}$$

$$(A.6) \quad \bar{k}_{12} = \frac{AR \left( \frac{1}{C_t} + \frac{1}{C_b} \right)}{m_b \Omega^2}$$

$$(A.7) \quad \bar{k}_2 = \frac{A^2 \left( \frac{1}{C_t} + \frac{1}{C_b} \right) + k_d}{m_b \Omega^2 R}$$

$$(A.8) \quad \bar{F} = \frac{F}{m_b \Omega^2 R^2}$$

$$(A.9) \quad \bar{k}_d = \frac{k_d}{m_b \Omega^2 R}$$

$$(A.10) \quad \bar{C}_t = \frac{C_t m_b \Omega^2}{R^3}$$

$$(A.11) \quad \bar{C}_b = \frac{C_b m_b \Omega^2}{R^3}$$

$$(A.12) \quad \bar{A} = \frac{A}{R^2}$$

## COPYRIGHT STATEMENT

The authors confirm that they, and/or their company or organization, hold copyright on all of the original material included in this paper. The authors also confirm that they have obtained permission, from the copyright holder of any third party material included in this paper, to publish it as part of their paper. The authors confirm that they give permission, or have obtained permission from the copyright holder of this paper, for the publication and distribution of this paper as part of the ERF proceedings or as individual offprints from the proceedings and for inclusion in a freely accessible web-based repository.